processes

MDPI

Article

Estimation of Multiple Parameters in Semitransparent Mediums Based on an Improved Grey Wolf Optimization Algorithm

Kefu Li [1,*], Lang Xie [1], Jianhua Zhou [1], Xiaofang Wu [1], Ding Ding [1] and Caibin Li [2]

[1] Architectural Engineering Institute, North China Institute of Aerospace Engineering, Langfang 065000, China
[2] Harbin Jicheng Automation Equipment Co., Ltd., Harbin 150078, China
* Correspondence: shendaozhan@163.com

Abstract: This work investigates the inverse coupled radiation–conduction problem for estimating thermophysical parameters and source terms by an improved grey wolf optimization (GWO). The transient coupled radiation–conduction heat transfer problem in participating slab media is solved by the finite volume method. The radiative intensities on both boundaries are adopted as known measurement information in the inverse model. To overcome the disadvantages of the original GWO algorithm, an improved grey wolf algorithm (IGWO) is developed by introducing the weight strategy and nonlinear factors. Three benchmark functions are adopted to prove that the IGWO has a faster convergence speed and higher estimation accuracy than the original one. The IGWO is applied to inverse the thermophysical parameters and source terms based on the coupled radiation–conduction model; the results indicate that the IGWO is accurate and effective for estimating refractive index, absorption coefficient, and source terms.

Keywords: improved grey wolf optimization; optical and thermal parameters; inverse radiation–conduction problem

Citation: Li, K.; Xie, L.; Zhou, J.; Wu, X.; Ding, D.; Li, C. Estimation of Multiple Parameters in Semitransparent Mediums Based on an Improved Grey Wolf Optimization Algorithm. *Processes* **2024**, *12*, 1445. https://doi.org/10.3390/pr12071445

Academic Editor: Chengtung Chou

Received: 10 May 2024
Revised: 3 July 2024
Accepted: 9 July 2024
Published: 10 July 2024

1. Introduction

The coupled radiation–conduction heat transfer (RCHT) in semitransparent media has a wide range of applications in engineering fields, such as combustion and flame propagation, solar photo-thermal conversion, remote sensing, stellar atmosphere detection, atmosphere science, aerospace engineering, fireproof materials, and phase change [1–11]. It is very important and necessary to understand the radiative energy transfer mechanism in these engineering applications, which relies greatly on the accurate knowledge of the optical and thermal parameters of the semitransparent materials. However, in many cases of practical interest, the optical and thermal parameters are commonly not known in advance and cannot be measured directly because it is difficult to probe internal media. To solve this problem, inverse heat transfer analysis is proposed by some scholars and applied in the estimation of the optical and thermal parameters including wall emissivity, scattering albedo, optical thickness, reflection, and absorption coefficients, to name a few [12–15].

To date, a great quantity of inverse techniques have been proposed and developed. Most of them can be divided into two groups: the gradient-based method (or deterministic algorithm) and the random-search-based method (stochastic-based optimization algorithm). The gradient-based methods, which include the conjugate gradient (CG) method [16] and the Levenberg–Marquardt (LM) method [17], have been applied to solve heat transfer problems. However, they refer to complicated mathematical calculations, and it is difficult to achieve a feasible solution without a reasonable initial value guess [18,19]. Moreover, the objective function must be known for these gradient-based methods. To

provide convenient and reliable solutions for inverse heat transfer problems, many scholars turn their attention to random-search-based methods, such as genetic algorithm (GA) [20], ant colony optimization (ACO) [21], particle swarm optimization (PSO) [22], glowworm swarm optimization (GSO) [23], and grey wolf optimization (GWO) [24]. Compared with the gradient-based method, these random-search-based methods have the following advantages: (1) The derivation of the objective function is not necessary; (2) it does not rely on an initial value; (3) the calculations are easy. In a word, the random-search-based method is more competitive than the gradient-based method in solving heat transfer problems.

Inspired by the predation behavior of the grey wolf group, the grey wolf optimization (GWO) was proposed by Mirjalili et al. [24] in 2014. The main idea of the GWO algorithm is the predation behavior of the grey wolf group based on the mechanism of wolf population coordination. The GWO algorithm has the characteristics of a simple structure, few parameters to be adjusted, and easy implementation. In addition, there are linear convergence factors and information feedback mechanisms that can be adjusted adaptively, which keeps the balance between local search ability and global search ability. With these characteristics, the GWO algorithm has great advantages for inverse problems. As far as the author's knowledge is concerned, the application of the GWO algorithm to inverse problems of the coupled RCHT in semitransparent media has not been reported. In this paper, the feasibility of applying the GWO algorithm to the inverse problems of the coupled RCHT in semitransparent media is discussed. To achieve faster convergence speed and higher accuracy, an improved grey wolf optimization (IGWO) based on a weighting strategy and nonlinear convergence factor is proposed. The population diversity of the initial grey wolf group is increased to some extent by increasing the population size of the grey wolf group. The convergence speed can be greatly improved by the weighting strategy. The linear convergence factor is replaced by the nonlinear convergence factor of the cosine curve to further balance the global search ability. Then, the IGWO is applied to inverse the optical parameters including refractive index, absorption coefficient, and source term based on the coupled radiation–conduction model. The other sections of this paper are organized as follows: The principle and detailed calculation of the basic GWO algorithm and the IGWO algorithm are given in Section 2. The results and discussions of inverse analysis are presented in Section 3. The main conclusions and perspectives are provided in Section 4.

2. GWO Algorithm

2.1. Original GWO Algorithm

The hunting behavior of the grey wolf group in nature is simulated in the original GWO algorithm. Each grey wolf represents a candidate, and the prey represents the sought solution. The group hunting including tracking prey, surrounding prey, and attacking prey is completed by the lowest-ranked ω wolves, which are led by higher-ranking α wolf, β wolf, and δ wolf in this algorithm. The social rank of the grey wolf group is shown in Figure 1. The GWO algorithm is inspired by the group's hunting behavior, and its mathematical model is established in this section. As shown in Figure 2, the group hunting behavior of grey wolves in the mathematical model can be summarized as surrounding prey, hunting, attacking prey, and searching for prey (exploration).

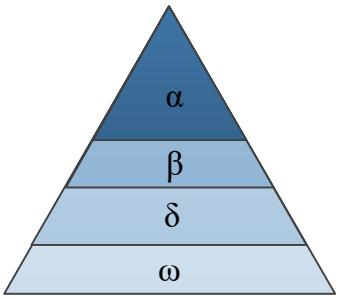

Figure 1. The social hierarchy of the grey wolf group.

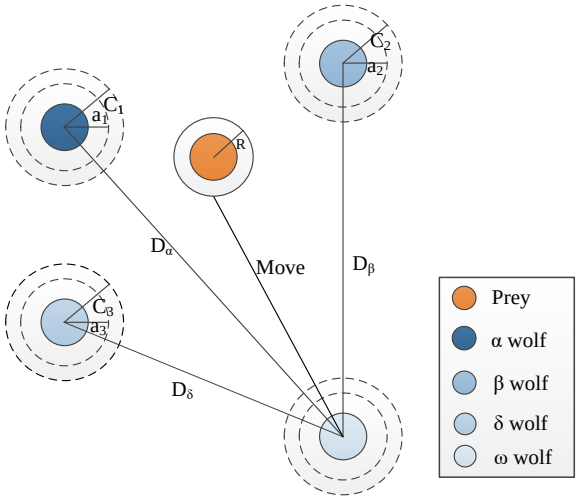

Figure 2. Position updating of the grey wolf in GWO.

The prey is tracked by the grey wolf group when it is found, and it will be quickly surrounded. The natural behavior can be expressed as the following mathematical calculations:

$$\begin{gathered}\mathbf{a}=\left(\mathbf{a}_{\text{ini}}-\mathbf{a}_{\text{fin}}\right)\cdot\left(\frac{t_{\max}-t}{t_{\max}}\right)\\ \mathbf{A}=2\cdot\mathbf{a}\cdot r_1-\mathbf{a}\\ \mathbf{C}=2\cdot r_2\end{gathered}\tag{1}$$

$$\mathbf{D}=\mathbf{C}\cdot\mathbf{X}_{\text{p}}-\mathbf{X}\tag{2}$$

$$\mathbf{X}\left(t+1\right)=\mathbf{X}_{\text{p}}\left(t\right)-\mathbf{A}\cdot\mathbf{D}\tag{3}$$

where $\mathbf{a}_{\text{ini}}$ and $\mathbf{a}_{\text{fin}}$ are the beginning and ending values of the control parameters, respectively, generally take 2 and 0. t is the current number of iterations, and $t_{\max}$ is the maximum number of iterations. $\mathbf{a}$ is the convergence factor; the $\mathbf{A}$ and $\mathbf{C}$ both are coefficient vectors; r_1 and r_2 are random numbers within [0, 1]. $\mathbf{X}$ and $\mathbf{X}_{\text{p}}$ are the positions of the grey wolves and the prey, respectively. The distance $\mathbf{D}$ between the grey wolves and the prey is defined in Equation (2), while the final position of the grey wolf $\mathbf{X}(t+1)$ is defined in Equation (3).

The prey is surrounded, and its position can be identified by the grey wolves. To simulate the collective hunting behavior of grey wolves, we assume that the α wolf, β wolf, and δ wolf have a better understanding of the potential position of prey. Therefore, the grey wolves with the best fitness value, suboptimal, and third best are the α wolf, β wolf, and δ wolf in each iteration, respectively, and their position information is automatically saved. Then, all the individuals of the grey wolf group are based on these three position

information, comprehensively judge the direction in which the individual moves to the prey, and update its position. The updated formula is as follows:

$$\begin{aligned} \mathbf{D}_{\alpha} &= \left|\mathbf{C}_1 \cdot \mathbf{X}_{\alpha} - \mathbf{X}\right| \\ \mathbf{D}_{\beta} &= \left|\mathbf{C}_2 \cdot \mathbf{X}_{\beta} - \mathbf{X}\right| \\ \mathbf{D}_{\delta} &= \left|\mathbf{C}_3 \cdot \mathbf{X}_{\delta} - \mathbf{X}\right| \end{aligned} \tag{4}$$

$$\begin{aligned} \mathbf{X}_1 &= \mathbf{X}_{\alpha} - \mathbf{A} \cdot \mathbf{D}_{\alpha} \\ \mathbf{X}_2 &= \mathbf{X}_{\beta} - \mathbf{A} \cdot \mathbf{D}_{\beta} \\ \mathbf{X}_3 &= \mathbf{X}_{\delta} - \mathbf{A} \cdot \mathbf{D}_{\delta} \end{aligned} \tag{5}$$

$$\mathbf{X}(t+1) = \left(\mathbf{X}_1 + \mathbf{X}_2 + \mathbf{X}_3\right)/3 \tag{6}$$

where the distance between the α wolf, β wolf, and δ wolf and other individuals is represented, respectively, by $\mathbf{D}_{\alpha}$, $\mathbf{D}_{\beta}$, and $\mathbf{D}_{\delta}$ in Equation (4). The current position of the α wolf, β wolf, and δ wolf are represented, respectively, by $\mathbf{X}_{\alpha}$, $\mathbf{X}_{\beta}$, and $\mathbf{X}_{\delta}$ in Equation (4). The calculation formulas in Equation (5) respectively represent the advancement and direction of the ω wolf to the α wolf, β wolf, and δ wolf. The final position of the ω wolf is defined in Equation (6).

When the prey stops moving, the hunting is completed by the grey wolf group through an attack. To simulate the process of approaching prey, the value of **a** gradually decreases, and the value of the **A** (A_j) also gradually decreases. The value of **a** decreases linearly from 2 to 0, and the A_j also varies within [−a, a]. When $|A_j| < 1$, the prey is attacked by the grey wolves. In addition, the grey wolves are separated from each other when searching for prey and gather together when attacking prey. The grey wolf can be forced to separate from the prey by $|A_j| > 1$, which emphasizes the role of exploration and strengthens the global search ability in the GWO algorithm. Moreover, the value of the **C** (C_j) is a random value between [0, 2] and can represent the random weight of the individual wolf's position on the prey. $C_j > 1$ means that the weight influence is significant, and conversely, the weight influence is small. The flow chart of the GWO algorithm is shown in Figure 3.

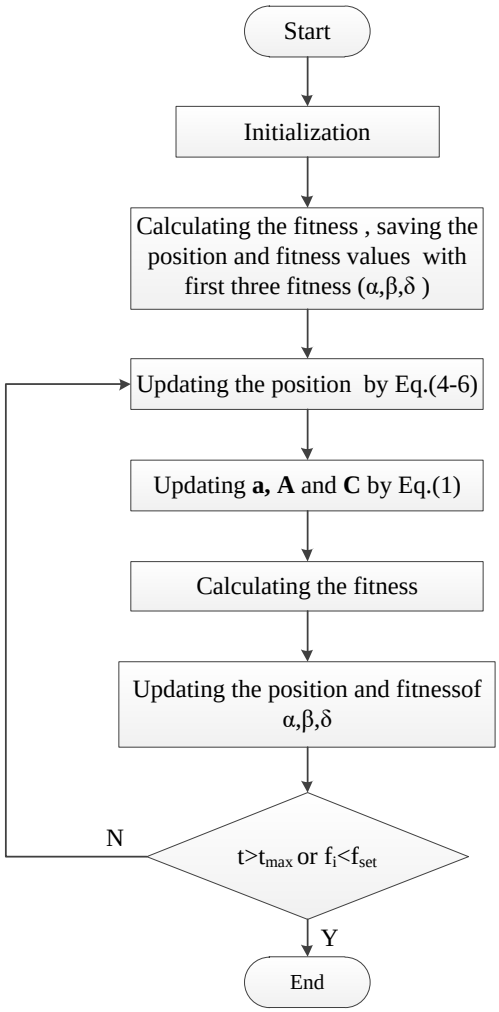

Figure 3. The flow chart of the GWO algorithm.

2.2. Improved GWO Algorithm

A great number of test functions are applied to test the performance of the GWO algorithm by Mirjalili [24]. According to the test results, it can be concluded that the GWO algorithm has the following disadvantages: (1) Poor population diversity. This is caused by the initial population generation. The population diversity is not guaranteed by randomly initializing. (2) The convergence rate is slower in the later stage, which is caused by the search mechanism of the GWO algorithm. The grey wolf group mainly judges the distance from the prey based on the distance from the α wolf, β wolf, and δ wolf, resulting in a slower convergence rate in the later stage. (3) The GWO algorithm makes it easy to achieve the local optimum because the α wolf does not necessarily represent the best global solution. In constant iteration, the ω wolf will continue to approach the α wolf, β wolf, and δ wolf, which leads to easily achieving the local optimum. In response to these shortcomings, many researchers have improved the GWO algorithm from four aspects: improvements in the initial population [25], improvements in the search mechanism [26], improvements in parameters [27], and the design of the hybrid algorithm [28,29].

Given the shortcomings of the GWO algorithm, an improved GWO (IGWO) algorithm is proposed in this paper. Firstly, the population diversity of the initial grey wolf group is increased to some extent by increasing the population size of the grey wolf group. Moreover, to overcome the disadvantage of slow convergence in the later stage, the convergence speed can be greatly improved by the weighting strategy. The calculations of the weighting strategy in the GWO algorithm are expressed as follows:

$$\begin{aligned} w_1 &= \mathbf{X}_1 / \left(\mathbf{X}_1 + \mathbf{X}_2 + \mathbf{X}_3 \right) \\ w_2 &= \mathbf{X}_2 / \left(\mathbf{X}_1 + \mathbf{X}_2 + \mathbf{X}_3 \right) \\ w_3 &= \mathbf{X}_3 / \left(\mathbf{X}_1 + \mathbf{X}_2 + \mathbf{X}_3 \right) \end{aligned} \tag{7}$$

$$\mathbf{X}(t+1) = \left(w_1 \cdot \mathbf{X}_1 + w_2 \cdot \mathbf{X}_2 + w_3 \cdot \mathbf{X}_3 \right) / 3 \tag{8}$$

To overcome the shortcoming of premature convergence in the GWO algorithm, the linear convergence factor **a** is replaced by the nonlinear convergence factor of the cosine curve to further balance the global search ability and the local search ability in the algorithm, which is calculated with the equation below. It is worth noting that for different algorithms, the selection of the nonlinear convergence factor is different.

$$\mathbf{a} = \left(\mathbf{a}_{\text{ini}} - \mathbf{a}_{\text{fin}} \right) \cdot \cos\left(\frac{t}{t_{\max}} \cdot \frac{\pi}{2} \right) \quad f_i < f_{\text{avg}} \tag{9a}$$

$$\mathbf{a} = \mathbf{a}_{\max} \qquad f_i \geq f_{\text{avg}} \tag{9b}$$

The flowchart of the IGWO algorithm is shown in Figure 4.

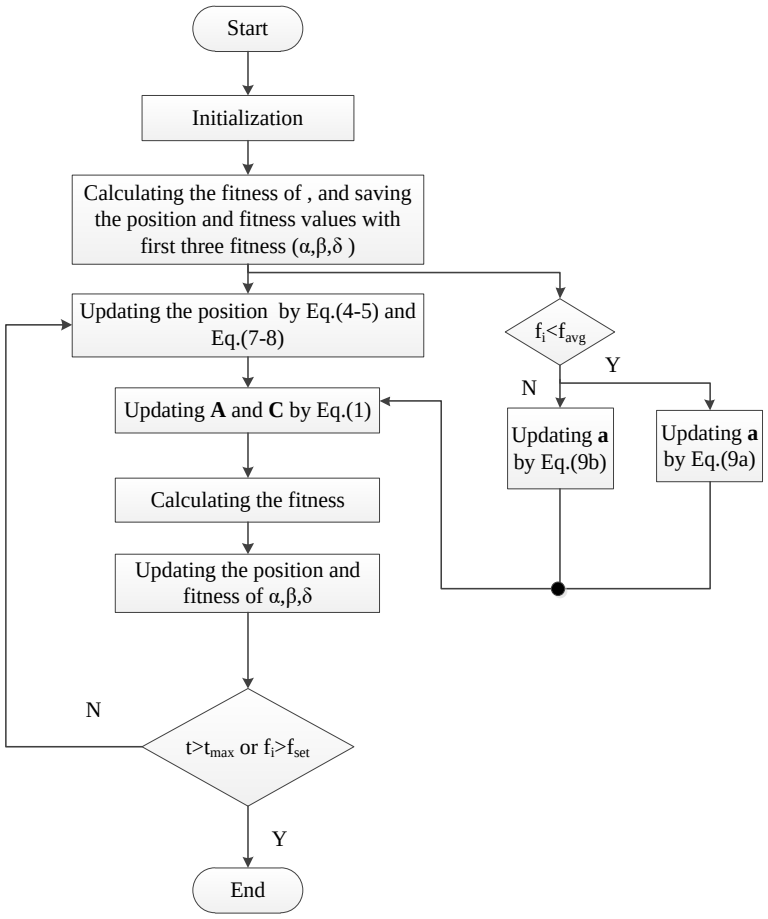

Figure 4. The flow chart of the IGWO algorithm.

2.3. Performance Test of IGWO Algorithm

Three well-known test functions are applied to test the performance of the IGWO algorithm in this paper, as shown in Table 1. The parameter settings in these two algorithms are as follows for all test functions: The maximum number of iterations is 500, the population size M is 100, and the values of a_{ini} and a_{fin} are set to 2 and 0, respectively. The average best fitness values of 10 independent run times for the three test functions and the corresponding standard deviation are listed in Table 2. The iterative curves of the best fitness of the GWO algorithm and the IGWO algorithm for these three test functions are shown in Figures 5–7.

Table 1. Details of test functions.

Function	Expression	Dimension	Space
Sphere	$f_1 = \sum_{i=1}^{n} x_i^2$	30	[−100, 100]
Rosenbrock	$f_2 = \sum_{i=1}^{n} \left[100\left(x_{i+1} - x_i^2\right)^2 + \left(x_i - 1\right)^2 \right]$	30	[−100, 100]
Griewank	$f_3 = \sum_{i=1}^{D} i x_i^2$	30	[−100, 100]

Table 2. Fixed Iteration results in 10 runs.

Function	GWO	Iteration	IGWO	Iteration
F1 (Sphere).	$3.03\times10^{-33} \pm 3.69\times10^{-34}$	500	$3.77\times10^{-50} \pm 3.69\times10^{-51}$	83
F2 (Rosenbrock)	27.0121 ± 1.0631	500	28.8766 ± 0.0623	500
F3 (Griewank)	$2.15\times10^{-31} \pm 3.10\times10^{-32}$	500	$2.45\times10^{-50} \pm 3.10\times10^{-51}$	86

The IGWO algorithm has better estimated values and better robustness than the GWO algorithm, as shown in Table 2. Anyway, as shown in Figures 5–7, the average fitness curve of the IGWO algorithm decreases faster than the GWO algorithm's. Compared to GWO, it is not easy for the IGWO to fall into a local optimal solution. Therefore, the fitness value drops to a lower level. The above results indicate that the IGWO algorithm converges faster than the GWO algorithm, the improvement of the GWO algorithm in this paper is remarkable.

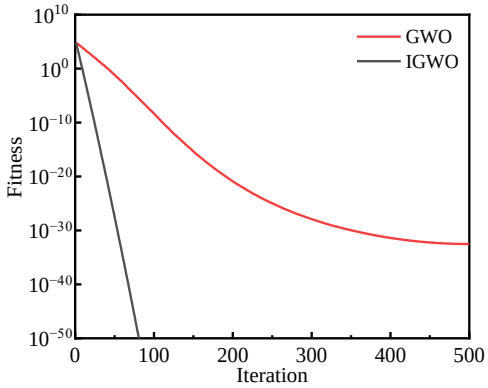

Figure 5. The comparison between GWO and IGWO for sphere function.

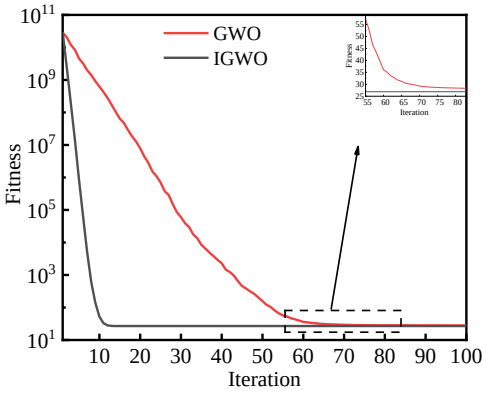

Figure 6. The comparison between GWO and IGWO for Rosenbrock function.

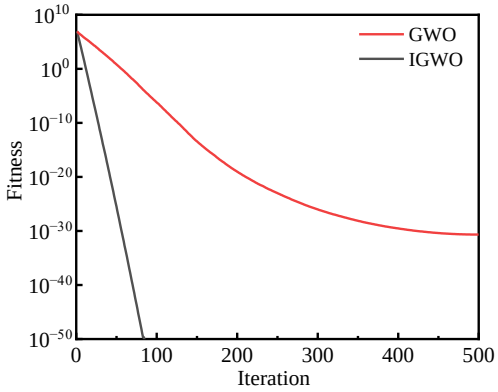

Figure 7. The comparison between GWO and IGWO for sum square function.

3. Results and Discussion

The IGWO algorithm is applied to estimate source term coefficients as well as refractive index and absorption coefficient in the coupled RCHT in semitransparent media. Measurement errors are unavoidable in practical applications. Therefore, the random standard deviation is added to the radiative signals obtained by the direct problem solver, which is expressed as

$$\mathbf{Y}_{\text{mea}} = \mathbf{Y}_{\text{exact}} + \sigma_0 \zeta \tag{10}$$

where $\mathbf{Y}_{\text{mea}}$ and $\mathbf{Y}_{\text{exact}}$ indicate the measured value and exact value of the measured signals (simulated by the direct model), which served as the input for inverse analysis. ζ is a random variable of normal distribution with zero mean and unit standard deviation. σ_0 has a 99% confidence level for a γ measurement error and is defined as follows:

$$\sigma_0 = \frac{Y_{\text{exact}} \times \gamma}{2.576} \tag{11}$$

where 2.576 indicates that 99% of a normally distributed population is contained within ± 2.576 standard deviation of the mean. γ is set as 0%, 3%, and 5% in this work. For comparison, the relative error ε_{rel} is defined as follows:

$$\varepsilon_{\text{rel}} = 100\% \times \frac{Y_{\text{est}} - Y_{\text{exact}}}{Y_{\text{exact}}} \tag{12}$$

In each case, the IGWO algorithm is implemented using FORTRAN code, INTEL I5-6200U PC.

3.1. Inverse Estimation for source term coefficients

The physical model of the 1D parallel slab with thickness τ_L bounded by two opaque, diffuse, and grey walls in semitransparent and grey media is shown in Figure 8. The left and right boundary walls are subjected to the first-type boundary condition with a constant temperature of T_{w1} and T_{w2}, respectively. For the case of only radiation without heat conduction, the radiative intensities can be expressed as follows [30]:

$$\begin{aligned} I^{+}(\tau,\mu) &= I_{b1}\exp\left[-(\tau_L-\tau)/\mu\right]+\frac{1}{\mu}\int_0^{\tau} S(\tau')\exp\left[-(\tau-\tau')/\mu\right]d\tau' \quad 0<\mu<1 \\ I^{-}(\tau,\mu) &= I_{b2}\exp\left[-(\tau_L-\tau)/\mu\right]-\frac{1}{\mu}\int_0^{\tau} S(\tau')\exp\left[-(\tau-\tau')/\mu\right]d\tau' \quad -1<\mu<0 \end{aligned} \tag{13}$$

with the boundary conditions as follows [30]:

$$\begin{aligned} &I_{b1}=I_{b2}=0 \\ &\tau=0 \quad -1\le\mu\le 0 \\ &\tau=\tau_L \quad 0\le\mu\le 1 \end{aligned} \tag{14}$$

where I_{b1} and I_{b2} denote the radiative intensities at the boundaries. μ is the directional cosine and $\mu = \cos\theta$. We can assume that the source term $S(\tau)$ is represented by a polynomial of the variable τ

$$S(\tau)=\sum_{i=1}^{D} a_i \tau^{i-1} \tag{15}$$

The thickness of the media is set as $\tau_L = 0.01$ m, and the temperature of the boundary walls is assumed to be $T_{w1} = 1000$ K and $T_{w2} = 1000$ K in this paper. The source term coefficients are expressed as $\mathbf{a}=[a_1,a_2,\ldots,a_n]^T$. The objective function is defined as follows:

$$\begin{aligned} F_{obj} = \left\| I_{mea}(\mathbf{a},\mu,0)-I_{est}(\mathbf{a},\mu,0)\right\|_{L_2} + \left\| I_{mea}(\mathbf{a},\mu,\tau_L)-I_{est}(\mathbf{a},\mu,\tau_L)\right\|_{L_2} \\ \tau=0 \quad -1\le\mu\le 0 \\ \tau=\tau_L \quad 0\le\mu\le 1 \end{aligned} \tag{16}$$

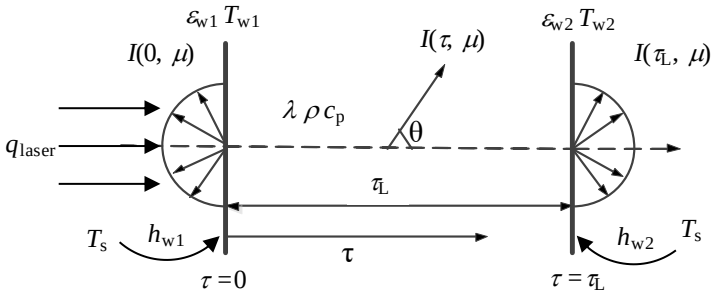

Figure 8. The physical model of the 1D parallel slab.

The IGWO algorithm is applied to estimate the source term coefficients. The source term coefficients are regarded as position **X** in IGWO. The fitness function converges by updating X step by step (See Figure 4 for details). The radiative intensities are calculated by Equations (13)–(15) in each iteration (a detailed description of the finite volume method for solving the radiative transfer equation is clarified in Section 3.2). Then, the fitness function in each iteration step is obtained by Equation (16). The source term coefficients are obtained when the maximum number of iterations is reached. The parameters in the IGWO algorithm are listed in Table 3. We consider the two cases of the source term coefficients: $\mathbf{a}=[3,14,-14]^T$, $\mathbf{a}=[5,12,-12]^T$. The algorithms run independently 10 times in

this study. The average values, standard deviation, and relative error of the two cases are shown in Table 4, and the estimated values of source term coefficients that vary with the number of runs are shown in Figure 9.

Table 3. The parameters of the IGWO algorithm.

Algorithm	a_{fin}	a_{ini}	t_{max}	M
IGWO	0	2	500	100

Table 4. The retrieval results of the source term coefficients.

Exact Value	Measure Error	a_1	ε_{rel} (%)	a_2	ε_{rel} (%)	a_3	ε_{rel} (%)
$a_1 = 3$	$\gamma = 0\%$	$2.9998 \pm 9.05 \times 10^{-4}$	6.67×10^{-3}	$14.0010 \pm 1.03 \times 10^{-2}$	7.37×10^{-2}	$-14.0016 \pm 1.07 \times 10^{-2}$	1.14×10^{-2}
$a_2 = 14$	$\gamma = 3\%$	$3.0003 \pm 8.11 \times 10^{-4}$	1.00×10^{-2}	$13.9979 \pm 9.81 \times 10^{-3}$	6.46×10^{-2}	$-13.9981 \pm 8.89 \times 10^{-3}$	1.36×10^{-2}
$a_3 = -14$	$\gamma = 5\%$	$2.9995 \pm 9.09 \times 10^{-4}$	1.67×10^{-2}	$14.0039 \pm 9.04 \times 10^{-3}$	7.00×10^{-2}	$-14.0039 \pm 9.71 \times 10^{-3}$	2.79×10^{-2}
$a_1 = 5$	$\gamma = 0\%$	$4.9999 \pm 1.30 \times 10^{-3}$	1.18×10^{-3}	$12.0008 \pm 1.57 \times 10^{-2}$	6.58×10^{-3}	$-12.0010 \pm 1.56 \times 10^{-2}$	8.13×10^{-3}
$a_2 = 12$	$\gamma = 3\%$	$4.9997 \pm 9.55 \times 10^{-4}$	5.54×10^{-3}	$12.0033 \pm 1.03 \times 10^{-2}$	2.75×10^{-2}	$-12.0032 \pm 1.03 \times 10^{-2}$	2.70×10^{-2}
$a_3 = -12$	$\gamma = 5\%$	$4.9997 \pm 9.76 \times 10^{-4}$	6.24×10^{-3}	$12.0046 \pm 1.11 \times 10^{-2}$	3.80×10^{-2}	$-12.0034 \pm 1.09 \times 10^{-2}$	2.83×10^{-2}

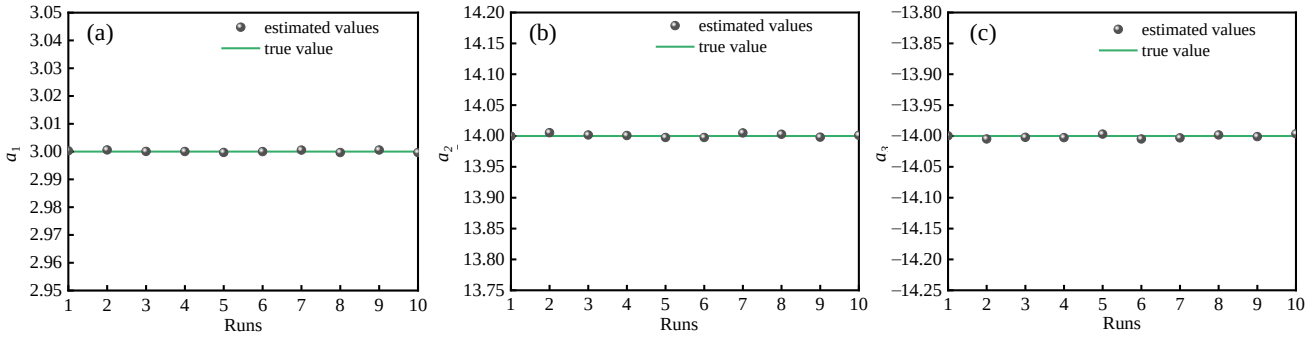

Figure 9. The estimate of (**a**) a_1, (**b**) a_2, and (**c**) a_3 varies with the number of runs.

As can be seen from Table 4, when measurement error γ = 5%, the biggest relative error is only 2.83 × 10^{-2}%. Moreover, the biggest standard deviation is still smaller than 0.1. Therefore, the IGWO algorithm has a high estimating accuracy and good stability for the source term coefficients. When the measurement error increases, the estimating accuracy decreases, but it can still be seen as a good estimating accuracy. During the 10 runs, the estimated value of the source term coefficients fluctuated to a small extent by the IGWO algorithm when the measurement error γ = 0% in Figure 9 shows that the estimation of the source term coefficients is reliable and stable. Therefore, the inverse estimation for the source term coefficients by the IGWO algorithm in this paper is successful.

3.2. Simultaneous Inverse Estimation of Refractive Index and Absorption Coefficient

3.2.1. Physical Model

For the reconstruction of radiative properties in participating media, the first and most essential stage is to solve the forward problem accurately and efficiently. The physical model of a 1D participating grey slab bounded by two opaque, diffuse, and grey walls in coupled RCHT in semitransparent media is shown in Figure 8. In this work, we assumed that the refractive index n and the absorption coefficient κ remain constant in the semitransparent media. The radiative transfer equation in 1D semitransparent pure absorption media can be written as follows [30,31]:

$$\frac{\mathrm{d}I(\tau,\mu)}{\mathrm{d}\tau} = -\kappa_a I(\tau,\mu) + n^2 \kappa_a I_b \tag{17}$$

where $I(\tau, \mu)$ is the radiative intensity at position τ and direction cosine μ, $\mu = \cos\theta$, θ means the polar angle. I_b is the blackbody radiative intensity at the temperature of media $T(\tau)$, n, and κ_a are the refractive index and the absorption coefficient, respectively. The energy transport process in semitransparent media can be described by an energy equation and a radiative transfer equation. The energy equation without internal heat generation can be written as [11]:

$$\rho c_p \frac{\partial T}{\partial t} = \lambda \frac{\partial^2 T}{\partial \tau^2} - \frac{\partial q^r}{\partial \tau} \tag{18}$$

where λ is the thermal conductivity, and ρc_P is the heat capacity. To obtain the refractive index and the absorption coefficient using an improved grey wolf optimization algorithm, the initial and boundary conditions are given as follows [11,30]:

$$\begin{gathered} T(\tau,0) = T_s \\ \varepsilon_{w1} q_{laser} + h_{w1}\left[T_s - T_{w1}(t)\right] + \varepsilon_{w1}\sigma\left[T_s^4 - T_{w1}^4(t)\right] = q_{w1}^r - \lambda \left.\frac{\partial T(t)}{\partial \tau}\right|_{x=0} \\ h_{w2}\left[T_s - T_{w2}(t)\right] + \varepsilon_{w2}\sigma\left[T_s^4 - T_{w2}^4(t)\right] = q_{w2}^r + \lambda \left.\frac{\partial T(t)}{\partial \tau}\right|_{x=L} \end{gathered} \tag{19}$$

where $\varepsilon_{w1}, \varepsilon_{w2}$ are the wall emissivity and σ is the Stefan–Boltzmann constant, q_{w1}^r, q_{w2}^r are the radiation heat flux of the left and right wall, and q_{laser} is the laser intensity. T_{w1} and T_{w2} are the temperatures of the left and right walls. T_s is the initial temperature or ambient temperature, and h_{w1}, h_{w2} are convective heat transfer coefficients. Then, the q_{w1}^r, q_{w2}^r and $(\partial q^r / \partial \tau)$ can be expressed as follows [11,30]:

$$\begin{gathered} q_{w1}^r = \varepsilon_{w1}\left[\sigma T_{w1}^4 - \int_{\cos\theta<0} 2\pi I(0,\mu)\,|\cos\theta|\sin\theta d\theta\right] \\ q_{w2}^r = \varepsilon_{w2}\left[\sigma T_{w2}^4 - \int_{\cos\theta>0} 2\pi I(\tau_L,\mu)\,|\cos\theta|\sin\theta d\theta\right] \\ \frac{\partial q^r}{\partial x} = 4\pi\kappa_a\left[I_b(\tau) - \frac{1}{2}\int_0^\pi I(\tau,\mu)d\theta\right] \end{gathered} \tag{20}$$

The finite volume method (FVM) is employed to solve Equations (17)–(20) in this work. The schematic of the control volume and neighbor nodes are illustrated in Figure 10. As for the energy equation, the left side of the equation and the diffusion term are discretized as follows [30]:

$$\int_t^{t+\Delta t}\int_w^e\int_s^n\int_b^f \rho c_p \frac{\partial T}{\partial t} dxdydzdt = (\rho c_p)_P \times (T_P - T_P^0) \times \Delta x\Delta y\Delta z \tag{21}$$

$$\begin{aligned} &\int_t^{t+\Delta t}\int_w^e\int_s^n\int_b^f \nabla\cdot(\lambda\nabla T)\,dxdydzdt \\ &= \left[\lambda_e\cdot\frac{T_E - T_P}{(\Delta x)^2} - \lambda_w\cdot\frac{T_P - T_W}{(\Delta x)^2} + \lambda_n\cdot\frac{T_N - T_P}{(\Delta y)^2} - \lambda_s\cdot\frac{T_P - T_S}{(\Delta y)^2} + \right. \\ &\left. \lambda_f\cdot\frac{T_F - T_P}{(\Delta z)^2} - \lambda_b\cdot\frac{T_P - T_B}{(\Delta z)^2}\right]\Delta x\Delta y\Delta z\Delta t \end{aligned} \tag{22}$$

The radiative transfer equation is discretized as follows [30]:

$$f^m\frac{\partial I^m}{\partial x} + g^m\frac{\partial I^m}{\partial y} + h^m\frac{\partial I^m}{\partial z} = -\kappa_a I^m + n^2\kappa_a I_b(\mathbf{r}) \tag{23}$$

where f^m, g^m, and h^m are the cosines of each of the three axes. The integral scheme of Equation (23) based on the control volume is as follows [30]:

$$\begin{aligned} &f^m\left(I_e^m - I_w^m\right)\Delta y\Delta z + g^m\left(I_n^m - I_s^m\right)\Delta x\Delta z + h^m\left(I_f^m - I_b^m\right)\Delta x\Delta y \\ &= -\kappa_{a,P} I_P^m \Delta x\Delta y\Delta z + n^2\kappa_{a,P} I_{b,P}\Delta x\Delta y\Delta z \end{aligned} \tag{24}$$

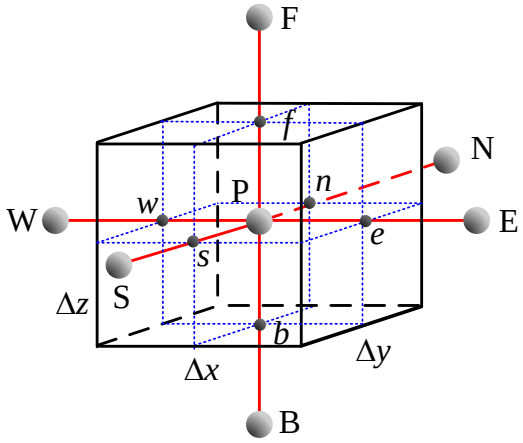

Figure 10. Schematic of control volume and neighbor nodes.

As for the one-dimensional model in this work, $\Delta y = \Delta z = 1$ and $x = \tau$. The initial boundary conditions and material properties are listed in Table 5.

Table 5. The parameter settings and boundary conditions for estimation of graded index.

Physical Parameters	Symbol	Value
The thickness of the medium	τ_L	0.01 m
The heat capacity	ρc_P	1.0×10^7 J/(m³·K)
The thermal conductivity	λ	0.7 W/(m·K)
The convective heat transfer coefficient	h_{w1}, h_{w2}	7.0 W/(m²·K)
Initial or ambient temperature	T_s	300 K
The laser intensity	q_{laser}	500 W/m²
The wall emissivity	$\varepsilon_{w1}, \varepsilon_{w2}$	1

3.2.2. Inverse Estimation of the Refractive Index and Absorption Coefficient

The objective function is defined as

$$F_{obj} = \left\| \frac{\mathbf{I}_{est}}{\mathbf{I}_{mea}} - 1 \right\|_{L_2} \tag{25}$$

where F_{obj} is the value of the objective function and $\mathbf{I}_{est}$ and $\mathbf{I}_{mea}$ are the estimated parameters and measured parameters (in this work, the parameters denote the refractive index and absorption coefficient), respectively.

The influence of population size on the estimation of absorption coefficient and refractive index is discussed firstly in this paper. Three cases of population size M = 30, 50, and 100 are tested to study the influence of population size on the estimation of absorption coefficient and refractive index. Measurement error γ = 0%, the experimental results are shown in Table 6 and Figure 11.

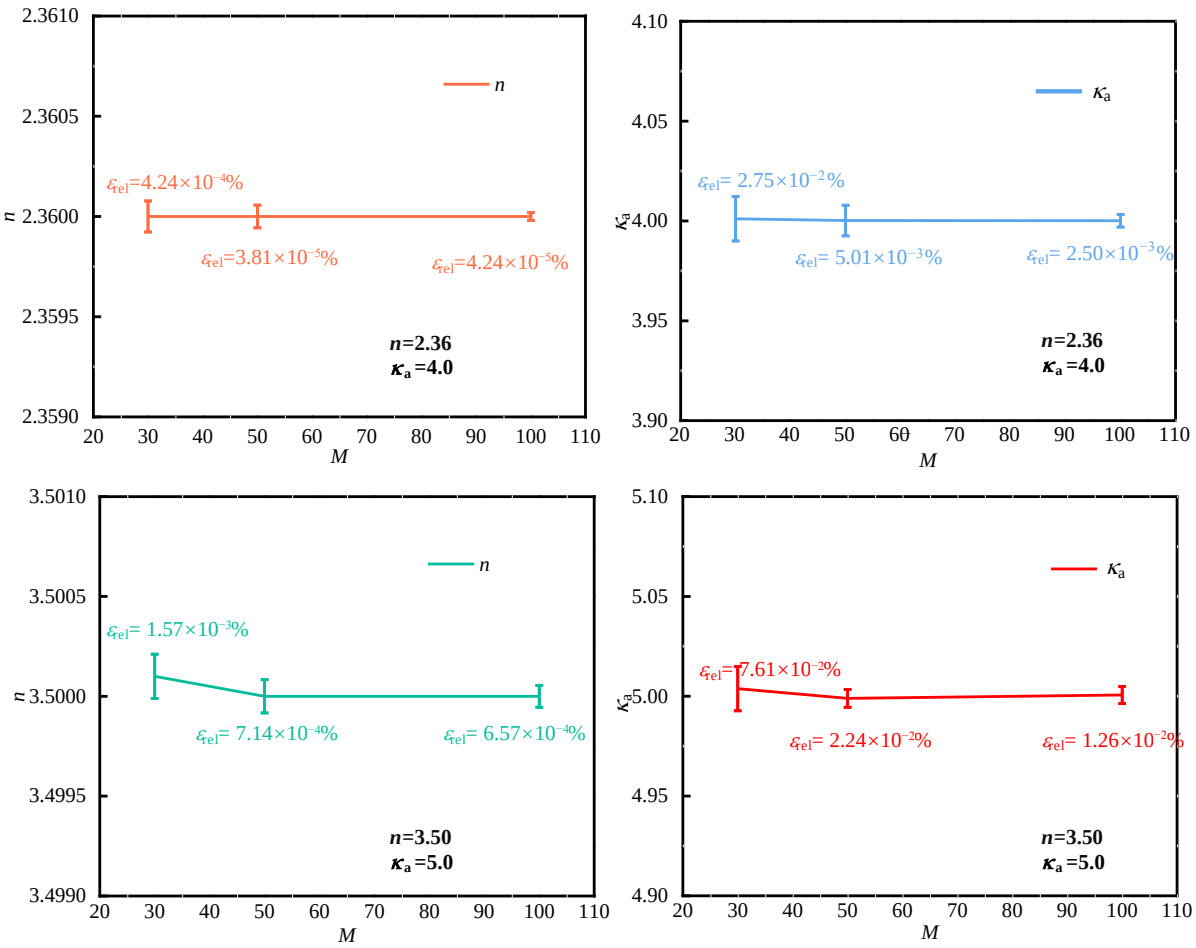

Figure 11. Estimation results of absorption coefficient and refractive index under different population sizes.

Table 6. Estimation results of different runs with different population sizes.

Runs	Population Size = 30				Population Size = 50				Population Size = 100			
	n	ε_{rel} (%)	κ_a	ε_{rel} (%)	n	ε_{rel} (%)	κ_a	ε_{rel} (%)	n	ε_{rel} (%)	κ_a	ε_{rel} (%)
1	2.36002	0.000847	4.00245	0.06125	2.36001	0.000424	3.99422	0.1445	2.36000	0	4.00102	0.0255
2	2.35994	0.002542	3.98836	0.291	2.36006	0.002542	4.01019	0.25475	2.36003	0.001271	4.00204	0.051
3	2.36009	0.003814	4.00454	0.1135	2.35990	0.004237	3.99224	0.194	2.36000	0	3.99930	0.0175
4	2.36012	0.005085	4.01512	0.378	2.36009	0.003814	3.99118	0.2205	2.35996	0.001695	3.99352	0.162
5	2.35997	0.001271	3.98440	0.39	2.35997	0.001271	3.99861	0.03475	2.36000	0	4.00135	0.03375
6	2.36006	0.002542	4.00759	0.18975	2.36002	0.000847	4.00334	0.0835	2.36001	0.000424	3.99957	0.01075
7	2.35998	0.000847	3.99912	0.022	2.36001	0.000424	3.99651	0.08725	2.35999	0.000424	3.99912	0.022
8	2.36000	0	4.00418	0.1045	2.35999	0.000424	3.99807	0.04825	2.36000	0	4.00124	0.031
9	2.36008	0.00339	4.01289	0.32225	2.35996	0.001695	3.99805	0.04875	2.35998	0.000847	3.99898	0.0255
10	2.35986	0.005932	3.99270	0.1825	2.35999	0.000424	3.99844	0.039	2.36002	0.000847	4.00045	0.01125

It can be seen from Figure 11 that the relative errors decrease with the increase in population size. Additionally, the trends in relative errors with the increasing running times show that the fluctuation of population size M = 100 is much less than that of the population size M = 30, 50, and its estimated average value is closer to the true value in Table 6, which indicates that increasing the population size can improve the stability of the estimated value and estimating accuracy. Therefore, the increase in population size is conducive to the estimation of the absorption coefficient and refractive index by the IGWO algorithm. To compare the results more intuitively, the subsequent results are illustrated in the table.

The IGWO algorithm estimates the absorption coefficient and refractive index with three different measurement errors γ = 0%, 3%, and 5%, and the results are shown in Tables 7 and 8 to verify the performance of the IGWO algorithm in a noisy environment. The population size is M = 30 and t_{max} = 500 in the three cases of measurement errors. The relative error of refractive index is only 4.24×10^{-4}% (the case of n = 2.36, κ_a = 4.0 m^{-1}) when measurement error γ = 0% in Table 7; therefore, the estimating accuracy is very high. If the population size is M = 100, the relative error of the refractive index will even drop to a lower level of 4.24×10^{-5}% when measurement error γ = 0% in Figure 11. As the measurement errors increase, the estimating accuracy decreases. However, the estimation value is still acceptable. When the measurement error γ = 5%, the relative error of the absorption coefficient is 3.84×10^{-1}% (the case of n = 3.50, κ_a = 5.0 m^{-1}), which is within a reasonable range. In addition, the estimated average values fluctuate more with the increasing measure errors in Table 8. All in all, the results show that the IGWO algorithm can estimate the absorption coefficient and refractive index with high accuracy and reliability even with noisy data.

Table 7. Estimation results of absorption coefficient and refractive index under different measurement errors.

Exact Value	Measure Error	ε_n	ε_{rel} (%)	κ_a	ε_{rel} (%)
n = 2.36 κ_a = 4.0	γ = 0%	$2.3600 \pm 7.78 \times 10^{-5}$	4.24×10^{-4}	$4.0011 \pm 1.11 \times 10^{-2}$	2.75×10^{-2}
	γ = 3%	$2.3610 \pm 1.31 \times 10^{-2}$	4.24×10^{-2}	$3.9965 \pm 9.01 \times 10^{-3}$	8.75×10^{-2}
	γ = 5%	$2.3686 \pm 1.28 \times 10^{-2}$	3.64×10^{-1}	$3.9932 \pm 3.81 \times 10^{-2}$	1.70×10^{-1}
n = 3.50 κ_a = 5.0	γ = 0%	$3.5001 \pm 1.11 \times 10^{-4}$	1.57×10^{-3}	$5.0038 \pm 1.11 \times 10^{-2}$	7.61×10^{-2}
	γ = 3%	$3.5036 \pm 2.13 \times 10^{-2}$	1.03×10^{-1}	$5.0067 \pm 1.67 \times 10^{-2}$	1.33×10^{-1}
	γ = 5%	$3.4953 \pm 3.65 \times 10^{-2}$	1.34×10^{-1}	$4.9808 \pm 1.96 \times 10^{-2}$	3.84×10^{-1}

Table 8. Estimation results of different runs with different measurement errors.

Runs	Measure Error = 0%				Measure Error = 3%				Measure Error = 5%			
	n	ε_{rel} (%)	κ_a	ε_{rel} (%)	n	ε_{rel} (%)	κ_a	ε_{rel} (%)	n	ε_{rel} (%)	κ_a	ε_{rel} (%)
1	2.36002	0.000847	4.00245	0.06125	2.35943	0.024153	3.99901	0.02475	2.36083	0.035169	3.97479	0.63025
2	2.35994	0.002542	3.98836	0.291	2.35652	0.147458	4.00351	0.08775	2.37942	0.822881	4.01223	0.30575
3	2.36009	0.003814	4.00454	0.1135	2.37278	0.541525	3.99553	0.11175	2.38106	0.892373	3.99321	0.16975
4	2.36012	0.005085	4.01512	0.378	2.35075	0.391949	3.99687	0.07825	2.39463	1.467373	4.01683	0.42075
5	2.35997	0.001271	3.98440	0.39	2.35259	0.313983	3.99507	0.12325	2.34236	0.747458	3.99695	0.07625
6	2.36006	0.002542	4.00759	0.18975	2.36087	0.036864	4.00166	0.0415	2.37423	0.602966	3.99618	0.0955
7	2.35998	0.000847	3.99912	0.022	2.36178	0.075424	3.99703	0.07425	2.36949	0.402119	4.04793	1.19825
8	2.36000	0	4.00418	0.1045	2.37068	0.452542	3.99690	0.0775	2.37773	0.751271	4.00493	0.12325
9	2.36008	0.00339	4.01289	0.32225	2.36673	0.285169	4.00650	0.1625	2.36561	0.237712	3.90035	2.49125
10	2.35986	0.005932	3.99270	0.1825	2.35481	0.219915	3.98811	0.29725	2.34342	0.702542	3.97317	0.67075

Finally, the influence of thermal conductivity is also studied in this paper. The cases of λ = 0.5, 0.7, and 0.9 W/(m·K) are discussed; the measurement error is γ = 0% and the population size is M = 100. The experimental results are shown in Tables 9 and 10. It can be seen from Table 9 that the relative errors increase with increasing thermal conductivity. In addition, the estimated average values fluctuate more with the increasing thermal conductivity in Table 10. Therefore, the decreasing thermal conductivity is helpful in improving the performance of the IGWO algorithm.

Table 9. Estimation results of absorption coefficient and refractive index with different thermal conductivities.

Exact Value	Thermal Conductivity	n	ε_{rel} (%)	κ_a	ε_{rel} (%)
n = 2.36 κ_a = 4.0	λ = 0.5	$2.3600 \pm 9.52 \times 10^{-5}$	6.36×10^{-4}	$4.0008 \pm 1.06 \times 10^{-2}$	1.97×10^{-2}
	λ = 0.7	$2.3600 \pm 7.78 \times 10^{-5}$	4.24×10^{-4}	$4.0011 \pm 1.11 \times 10^{-2}$	2.75×10^{-2}
	λ = 0.9	$2.3600 \pm 9.23 \times 10^{-5}$	1.44×10^{-3}	$4.0087 \pm 2.31 \times 10^{-2}$	2.18×10^{-1}

n = 3.50 κ_a = 5.0	λ = 0.5	$3.5000 \pm 1.47 \times 10^{-4}$	1.26×10^{-3}	$5.0036 \pm 9.36 \times 10^{-3}$	7.22×10^{-2}
	λ = 0.7	$3.5001 \pm 1.11 \times 10^{-4}$	1.57×10^{-3}	$5.0038 \pm 1.11 \times 10^{-2}$	7.61×10^{-2}
	λ = 0.9	$3.4956 \pm 1.41 \times 10^{-2}$	1.26×10^{-1}	$5.0056 \pm 3.94 \times 10^{-2}$	1.12×10^{-1}

Table 10. Estimation results of different runs with different thermal conductivities.

Runs	Thermal Conductivity = 0.5				Thermal Conductivity = 0.7				Thermal Conductivity = 0.9			
	n	ε_{rel} (%)	κ_a	ε_{rel} (%)	n	ε_{rel} (%)	κ_a	ε_{rel} (%)	n	ε_{rel} (%)	κ_a	ε_{rel} (%)
1	2.36	0	4.00141	0.03525	2.36002	0.000847	4.00245	0.06125	2.36005	0.002119	3.99955	0.01125
2	2.36006	0.002542	4.00936	0.234	2.35994	0.002542	3.98836	0.291	2.36012	0.005085	3.98836	0.291
3	2.36003	0.001271	4.00454	0.1135	2.36009	0.003814	4.00454	0.1135	2.36016	0.00678	4.01749	0.43725
4	2.35996	0.001695	4.0048	0.12	2.36012	0.005085	4.01512	0.378	2.36022	0.009322	4.01512	0.378
5	2.35999	0.000424	3.99879	0.03025	2.35997	0.001271	3.98440	0.39	2.36012	0.005085	4.01273	0.31825
6	2.35992	0.00339	3.99398	0.1505	2.36006	0.002542	4.00759	0.18975	2.36013	0.005508	4.02681	0.67025
7	2.35998	0.000847	3.99912	0.022	2.35998	0.000847	3.99912	0.022	2.36007	0.002966	4.00884	0.221
8	2.36	0	4.00418	0.1045	2.36000	0	4.00418	0.1045	2.35983	0.007203	3.9611	0.9725
9	2.35998	0.000847	3.99766	0.0585	2.36008	0.00339	4.01289	0.32225	2.36008	0.00339	4.01289	0.32225
10	2.36	0	3.99965	0.00875	2.35986	0.005932	3.99270	0.1825	2.36019	0.008051	4.05203	1.30075

4. Conclusions

Compared with the GWO algorithm, three well-known test functions are applied to test the performance of the IGWO algorithm. The results indicate that the average fitness curve of the IGWO algorithm, based on the weighting strategy and nonlinear convergence factor, decreases faster than the GWO algorithm. Moreover, it does not fall easily into the local optimal solution; the fitness value drops to a lower level. Therefore, the improvement of the GWO algorithm in this paper is remarkable. Then, the inverse coupled radiation–conduction heat transfer in semitransparent media is studied, the results indicate that the IGWO algorithm is applied to estimate the source term coefficients, absorption coefficient, and refractive index of the 1D participating grey slab in this paper. The experimental results show that the IGWO algorithm performs well in the estimation even with noisy data. In addition, the influence of population size and thermal conductivity are discussed in this paper, and the increasing population size and the decreasing thermal conductivity are helpful in improving the performance of the IGWO algorithm. In conclusion, the IGWO algorithm is relatively successful in the estimation of these three kinds of parameters and may be further applied to the estimation of other optical and thermal parameters.

Author Contributions: Conceptualization, K.L.; methodology, C.L.; software, L.X.; validation, D.D.; formal analysis, J.Z.; data curation, X.W. All authors have read and agreed to the published version of the manuscript.

Funding: The support of this work by the Project of Langfang Science and Technology Bureau (2021011083), North China Institute of Aerospace Engineering Doctoral fund (BKY-2020-41), and Science and Technology Project of Hebei Education Department (ZD2022112) are gratefully acknowledged.

Data Availability Statement: The original contributions presented in the study are included in the article, further inquiries can be directed to the corresponding author.

Acknowledgments: A very special acknowledgment is also made to the editors and referees who make important comments to improve this paper.

Conflicts of Interest: Caibin Li is employed by the Harbin Jicheng Automation Equipment Co., Ltd. company; the remaining authors declare that the research was conducted in the absence of any commercial or financial relationships that could be construed as a potential conflict of interest.

Nomenclature

Nomenclature		Greek symbols	
A	Coefficient vector	κ_s	The scattering coefficient

C	Coefficient vector	θ	The polar angle
D	Distance between grey wolf and prey	κ	Absorption coefficient
X	Grey wolf position	τ	Optical thickness
$\mathbf{X}_P$	Prey position	ε	Stefan- The wall emissivity
t	Number of iterations	σ	Stefan-Boltzmann constant
a	Convergence factor	λ	Thermal conductivity
r_1	Random number within [0, 1]	q^r	Power density
r_2	Random number within [0, 1]	ε_{rel}	The relative error
I	Radiative intensity	γ	The measurement error
n	Refractive index	**Subscripts**	
T	Temperature	mea	The measured value
q	Array radiative	est	The estimated value
F_{obj}	Objective function	exact	The exact value
Y	The estimated or exact values of refractive index, absorption coefficient, and source term	b	Black body
S	The source term	avg	Average value
a_n	The source term coefficient	L_2	L_2-type norm
M	The population size of grey wolf	i	The ith iteration

References

1. Viskanta, R.; Mengüç, M.P. Radiation heat transfer in combustion systems. *Prog. Energy Combust. Sci.* **1987**, *13*, 97–160.
2. Lockwood, F.C.; Shah, N.G. A new radiation solution method for incorporation in general combustion prediction procedures. *Symp. Combust.* **1981**, *18*, 1405–1414.
3. Al-Gebory, L.; Mengüç, M.P.; Koşar, A.; Şendur, K. Effect of electrostatic stabilization on thermal radiation transfer in nanosuspensions: Photo-thermal energy conversion applications. *Renew. Energy* **2018**, *119*, 625–640.
4. Mätzler, C. *Thermal Microwave Radiation: Applications for Remote Sensing*; Institution of Engineering & Technology: Guwahati, India, 2006; pp. 52–584.
5. Nordlund, Å.; Stein, R.F. Accurate radiation hydrodynamics and MHD modeling of 3-D stellar atmospheres. *AIP Conf. Proc.* **2009**, *1171*, 242–259.
6. Wiscombe, W.J.; Ramanathan, V. The role of radiation and other renascent subfields in atmospheric science. *Bull. Am. Meteorol. Soc.* **2010**, *66*, 1278–1287.
7. Tyshchenko, V.A.; Shabalina, T.N.; Sheikina, N.A.; Diskina, D.E. Radiation stability of low-viscosity base oils for aerospace engineering control systems, *Chem. Technol. Fuels Oils* **2003**, *39*, 141–144.
8. Song, X. Analysis of zirconium just jade nature fire-proof material by X-ray fluorescence spectrometry. *Chin. J. Spectrosc. Lab.* **2006**, *23*, 1314–1317.
9. Cheng, Q.; Chai, J.; Zhang, Z. Investigation of double-layer coating pigmented with CuO particles of different concentrations on aesthetic and thermal aspects. *Int. J. Therm. Sci.* **2016**, *105*, 36–44.
10. Wang, Z.C.; Song, J.L.; Chai, J.L.; Cheng, Q.; Zhou, H.C. The effect of BRDF surface on radiative heat transfer within a one-dimensional graded index medium. *Int. J. Therm. Sci.* **2014**, *77*, 116–125.
11. Wei, L.Y.; Qi, H.; Niu, Z.T.; Wen, S.; Ren, Y.T. Inverse heat transfer analysis to determine the temperature or phase change-dependent refractive index of semitransparent materials. *Inverse Probl. Sci. Eng.* **2021**, *29*, 586–608.
12. Wang, J.Y.; Gao, Z.X.; Lee, C.H. An iterative technique for coupled conduction-radiation heat transfer in semitransparent media. *Numer. Heat Transf. Part A Appl.* **2015**, *67*, 1208–1231.
13. Lacroix, D.; Parent, G.; Asllanaj, F.; Jeandel, G. Coupled radiative and conductive heat transfer in a non-grey collimated radiation. *J. Quant. Spectrosc. Radiat. Transf.* **2002**, *75*, 589–609.
14. An, W.; Zhu, T.; Gao, N.P. Accelerative iteration for coupled conductive-radiative heat transfer computation in semitransparent media. *Int. J. Heat Mass Transf.* **2015**, *82*, 503–509.
15. Bai, D.; Fan, X.J. Transient coupled heat transfer in multilayer non-gray Radiative heat transfer in semitransparentsolidifying slab considering space-time dependent refractive index media with reflective foils. *Int. J. Thermophys.* **2006**, 27, 647–664.
16. Li, H.Y. Inverse radiation problem in two-dimensional rectangular media. *J. Thermophys. Heat Transf.* **1997**, *11*, 556–561.

17. Menguc, M.P.; Manickavasagam, S. Inverse radiation problem in axisymmetric cylindrical scattering media. *J. Thermophys. Heat Transf.* **1993**, *7*, 479–486.
18. Chopade, R.P.; Agnihotri, E.; Singh, A.K.; Kumar, A.; Uppaluri, R.; Mishra, S.C.; Mahanta, P. Application of a particle swarm algorithm for parameter retrieval in a transient conduction-radiation problem. *Numer. Heat Transf. Part A Appl.* **2011**, *59*, 672–692.
19. Qi, H.; Niu, C.Y.; Gong, S.; Ren, Y.T.; Ruan, L.M. Application of the hybrid particle swam optimization algorithms for simultaneous estimation of multi-parameters in a transient conduction-radiation problem. *Int. J. Heat Mass Transf.* **2015**, *83*, 428–440.
20. Bonabeau, E.; Dorigo, M.; Theraulaz, G. *Swarm Intelligence: From Natural to Artificial Systems*; Oxford University Press: Oxford, UK, 1999.
21. Stutzle, T.; Dorigo, M. *Ant Colony Optimization*; Bradford Company: Holland, MI, USA, 2004.
22. Kennedy, J.; Eberhart, R. Particle swarm optimization, In Proceedings of the IEEE International Conference, Perth, WA, Australia, 27 November–1 December 1995; pp. 1942–1948.
23. Kaipa, K.N.; Ghose, D. *Glowworm Swarm Optimization: THEORY, Algorithms, and Applications*; Springer: Berlin/Heidelberg, Germany, 2017.
24. Mirjalili, S.; Mirjalili, S.M.; Lewis, A. Grey wolf optimizer. *Adv. Eng. Softw.* **2014**, *69*, 46–61.
25. Madhiarasan, M.; Deepa, S.N. Long-Term Wind Speed Forecasting using Spiking Neural Network Optimized by Improved Modified Grey Wolf Optimization Algorithm. *Int. J. Adv. Res.* **2016**, *4*, 356–368.
26. Gholizadeh, S. Optimal design of double layer grids considering nonlinear behavior by sequential grey wolf algorithm. *J. Optim. Civ. Eng.* **2015**, *5*, 511–523.
27. Long, W.; Liang, X.; Cai, S.; Jao, J.; Zhang, W. A Modified augmented Lagrangian with improved grey wolf optimization to constrained optimization problem. *Neural Comput. Plications* **2016**, *28*, 1–18.
28. Zhang, S.; Luo, Q.F.; Zhou, Y.Q. Hybrid grey wolf optimizer using elite opposition-based learning strategy and simplex method. *Int. J. Comput. Intell. Appl.* **2017**, *16*, 1750012.
29. Zhu, A.; Xu, C.; Li, Z.; Wu, J; Liu, Z. Hybridizing grey wolf optimization with differential evolution for glbal optimization and test scheduling for 3D stacked SoC. *J. Syst. Eng. Electron.* **2015**, *26*, 317–328.
30. Modest, M.F. *Radiative Heat Transfer*; McGraw-Hill: Now York, NY, USA, 2003.
31. Wei, L.Y.; Qi, H.; Zhang, X.L.; Wen, S.; Islam, M.A.; Ruan, L.M. Reconstruction of radiative properties fields in participating media by using the sequential quadratic programing combined with regularization technique. *J. Heat Transf.* **2019**, *141*, 022702.